# Improving Ego-Velocity Estimation of Low-Cost Doppler Radars for Vehicles

Aaron Kingery , Member, IEEE, and Dezhen Song, Senior Member, IEEE

Abstract—A low-cost automotive radar is often used in autonomous driving and advanced driver-assistance systems. However, the low cost radar often assumes all detected objects to be on the ground plane when estimating radar/vehicle ego-velocity, but when there are elevated background objects present, such as buildings and tall trees, the ego-velocity estimation tends to be biased. Here we analyze the source of estimation error and develop a new algorithm to recognize three types of object reflections using the discrepancy between the estimated ego-velocity and the measured Doppler velocity. We propose an elevation and background aware cost (EBAC) function to formulate an optimization framework which can distinguish the object types to improve ego-velocity estimation. We combine a robust estimation method with the optimization framework to handle outliers in radar readings. We have implemented the algorithm and tested it in both simulation and physical experiments using our autonomous vehicle. The results show that our estimation method significantly reduces ego-velocity estimation error while maintaining a smaller error variance without losing robustness. More specifically, it reduces the ego-velocity estimation error by 49% in the most common driving scenario.

Index Terms—Autonomous vehicle navigation, localization, range sensing.

# I. INTRODUCTION

N AUTONOMOUS driving or advanced driver-assistance systems (ADAS), Radio Detection and Ranging, colloquially known as radar, is one of the most frequently used sensors because they are insensitive to environmental conditions such as weather or lighting. They are considered as one of most important navigation sensors on-board a modern vehicle. Due to cost considerations, an automotive radar can often only perform horizontal scanning and cannot perceive target elevation. Such automotive radars rely on the Doppler effect to detect objects and estimate their relative velocities by assuming all objects are co-planar. However, when a vehicle traverses in urban streets, there are elevated background buildings reflecting radar signals which causes velocity estimation to be deviated from its true value (see Fig. 1). Such issues may not be a concern if the radars are only used for obstacle/collision avoidance. However, those

Manuscript received 1 March 2022; accepted 22 June 2022. Date of publication 15 July 2022; date of current version 26 July 2022. This letter was recommended for publication by Associate Editor K. Sohn and Editor H. Moon upon evaluation of the reviewers' comments. This work was supported in part by National Science Foundation under Grant NRI-1925037, in part by GM/SAE AutoDrive Challenge, and in part by the U.S. Department of Transportation/FHA under Grant 693JJ19NF00001. (Corresponding author: Dezhen Song.)

The authors are with the CSE Department, Texas A&M University, College Station, TX 77843 USA (e-mail: aaronmkingery@tamu.edu; dzsong@cs.

Digital Object Identifier 10.1109/LRA.2022.3191247

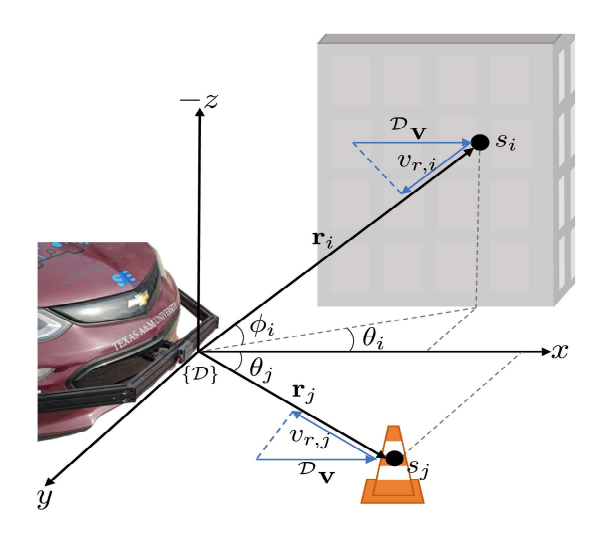


Fig. 1. The radar coordinate system and notations featuring two target detections one  $s_i$  is elevated, and another  $s_j$  is on the horizontal plane (i.e.  $\phi_j = 0$ ). Blue vectors indicate the velocity components. As can been seen from the geometry, the elevation angle of the target affects the target Doppler velocity.

radars are an attractive option for autonomous driving, especially for localization and mapping in all weather conditions. If we are to use those radars to perform accurate localization and mapping, the issues are not negligible.

Here we present a new, unsupervised ego-velocity estimation method to allow a low-cost Doppler radar to obtain accurate ego-velocity estimation. We analyze the Doppler radar working principle and propose an Elevation and Background Aware Doppler Cost (EBAC) to capture model discrepancy caused by different types of objects. By making use of the EBAC function, we can identify target types and recover the correct ego-velocity. To handle the outliers, we combine the random sample consensus (RANSAC) with Orthogonal Distance Regression (ODR) techniques to obtain robust and accurate ego-velocity estimation.

We have implemented the proposed algorithm and tested in both simulation and field experiments with an autonomous vehicle. The experimental results have shown significant improvements in ego-velocity estimation while maintaining a smaller error variance without losing robustness. More specifically, the results show that our estimation method can reduce ego-velocity estimation error by 49% in the most common driving scenario.

## II. RELATED WORK

Radar was first developed during the 1920 s and matured as a technology during the period just before and during WWII.

2377-3766 © 2022 IEEE. Personal use is permitted, but republication/redistribution requires IEEE permission. See https://www.ieee.org/publications/rights/index.html for more information.

The use of radar as sensor in the automotive space has a much shorter history. The modern 77 GHz automotive radar, like the one used for this work, was proposed by Langer [1] in 1996.

Automotive radar has been used for vehicle navigation since the earliest examples in the literature. Clark and Durrant-Whyte [2] employ automotive radar as part of an Extended Kalman Filter (EKF) fusion of steering encoder, wheel encoder, and radar target tracking for vehicle localization, wherein predesigned, preplaced beacons were tracked from the radar range and bearing measurements to estimate the vehicles relative position. Clark and Dissanayake [3] develop a Simultaneous Localization and Mapping (SLAM) algorithm using the automotive radar to map naturally radar reflective features in the environment and simultaneously localize within the map of radar target detections and Dissanayake et al. [4] describe an implementation of the SLAM algorithm using automotive radar to provide relative map observations. Schuster et al. [5] employ GraphSLAM [6] with radar detections as features to develop a radar SLAM algorithm. Those radar SLAM algorithm depends on accurate ego-velocity estimation which can be improved by applying our method.

In addition to tracking the strongest radar signal returns as target detections, image processing techniques have been used on the radar power spectrogram rendered as an image, especially for Frequency Modulated Continuous Wave (FMCW) radars which rotate to capture a 360° image of the environment. Checchin et al. [7] use the Fourier-Mellin Transform for image registration in order to estimate the relative pose between scans. Vivet et al. [8] analyze the relative distortion between pairs of successive radar scans in order to estimate the velocity and angular velocity of a ground based vehicles as well as a boat. Cen and Newman [9], [10] extract radar targets and propose a novel data association method for point set registration between successive radar scans in order to estimate the vehicle motion. Werber et al. [11] identify straight line segments, common in man-made environments, and associate them between successive scans for use as landmarks in radar based localization.

More recent developments have made use of the target Doppler velocity measurements provided by modern automotive radars in order to estimate the sensor's own ego-velocity. These methods are referred to as "instantaneous," because they estimate the ego-velocity from a single radar scan. Kellner et al. [12] create a model of the relative Doppler velocity of static, planar radar target detections and use the random sample consensus (RANSAC) algorithm [13] in order to robustly identify the static and dynamic targets, estimate the sensor's ego-velocity, and apply it to a single track vehicle model with Ackerman steering properties in order to estimate the vehicle longitudinal velocity and yaw rate. Subsequently, their approach has become the standard technique for estimating radar ego-velocity upon which our work improves by considering the effect of the target elevations on the relative Doppler velocities of target detections. Kellner et al. [14] further extend their approach to fuse the data from multiple Doppler radars and employ Orthogonal Distance Regression (ODR) [15] as a final re-optimization step to improve the estimate of the sensor ego-velocity. Steiner et al. [16] use many simpler single channel Doppler radars, which do not

have the capability to measure target azimuth, to estimate the radars' ego-velocities. Cho *et al.* [17], [18] develop a novel complex-valued neural network in order to estimate the radar ego-velocity.

Joint methods of fusing the estimated ego-velocity estimation from Doppler velocity analysis and analysis of target spatial distributions between successive frames have now become the state of the art for radar ego-motion estimation. Barjenbruch et al. propose the first such method fusing the ego-velocity estimation algorithm of Kellner et al. [12] and a point set registration algorithm to estimate the radar ego-velocity and subsequently the vehicle motion. Monaco and Brennan [19] propose the RADAR-ODO algorithm which uses the algorithm of Kellner et al. [12] to estimate the radar's translational motion and analysis of successive radar power spectrograms in order to estimate the radar's rotational motion allowing the radar ego-motion information to be used for vehicle motion estimation without the Ackermann steering constraint. Our work can be applied in these approaches to further improve the results by accounting for the target elevations in the ego-velocity estimation step.

### III. PROBLEM FORMULATION

Before we introduce our radar ego-velocity estimation problem, let us begin with the definition of coordinate systems, also known as frames.

- {D} is the dynamic radar ego-coordinate system which
  moves with the radar, it is a right-handed coordinate system
  defined such that the X-axis is forward, Y-axis is to the
  right, and the Z-axis is downward from the radar perspective.
- {W} is the static global inertial coordinate system, aligned with {D} at its initial position.

A left superscript of the coordinate frame indicates the coordinate perspective, e.g.  $^{\mathcal{D}}x$  would be the variable x from the coordinate perspective  $\{\mathcal{D}\}$ .

# A. Radar Inputs

Our sensor is a 77 GHz automotive Doppler radar which periodically transmits a pulse and reports a set of the received reflections as estimated target detections. We use  $D = \{s_1, \ldots, s_n\}$  to denote the set of target detections received as a datagram from a transmitted radar pulse. Each target detection is reported in polar coordinates in the radar coordinate frame  $\{\mathcal{D}\}$  and consists of the measurements

$$s_i = \left[ r_i \ \theta_i \ v_{r,i} \right]^\mathsf{T} \in D, \tag{1}$$

where,  $i \in \{1,\dots,n\}$  is target index,  $r_i$  is the i-th target range,  $\theta_i \in (-\pi,\pi]$  is the i-th target azimuth where  $\theta_i = 0$  indicates the forward direction (see Fig. 1),  $\theta_i < 0$  indicates a target to the left, and  $\theta_i > 0$  indicates a target to the right, and the Doppler velocity  $v_{r,i}$  which is the radial component of the relative velocity of the target where  $v_{r,i} < 0$  indicates a target moving radially towards the radar and  $v_{r,i} > 0$  indicates a target moving radially away from the radar. The sensor also provides estimated measurement error variances,  $\sigma_{r,i}^2$ ,  $\sigma_{\theta,i}^2$ , and  $\sigma_{v_r,i}^2$  respectively.

To facilitate our analysis, we additionally consider the target elevation which is not directly observed by the low cost Doppler radar, because it only does horizontal scanning. We define the target elevation to be  $\phi_i \in [-\phi_{\max},\phi_{\max}]$ , which is the angle of the target with respect to the radar horizontal plane where  $\phi_i < 0$  indicates a target below the horizontal plane,  $\phi_i > 0$  indicates a target above the horizontal plane, and  $\phi_{\max}$  is equal to half the radar's elevation beam width (see Fig. 1).

### B. Assumptions

We make the following assumptions throughout the paper:

- a.1 The radar is mounted such that its horizontal plane is parallel to the ground surface.
- a.2 The ground surface can be reasonably approximated by a plane. In an automotive application, this assumption holds in most cases. In conjunction with a.1, we can say that the radar's vertical velocity is approximately zero, i.e.  ${}^{\mathcal{D}}v_z\approx 0$ .
- a.3 Each component of  $s_i$  is independently distributed and therefore we can say that  $\Sigma_{s_i} = \mathrm{Diag}(\sigma_{r,i}^2, \sigma_{\theta,i}^2, \sigma_{v_r,i}^2)$ . We base this assumption on the fact that each measurement is of an independent quality of the received signal reflection, namely: time of flight for  $r_i$ , relative signal phase between radar receiver (RX) antennas for  $\theta_i$ , and Doppler frequency shift for  $v_{r,i}$ .
- a.4 The radar datagram contains a majority of static (i.e. non-moving) target detections. For the radar used in this work, the horizontal field-of-view is  $\pm 60^{\circ}$ , the vertical field-of-view is  $\pm 10^{\circ}$ , and the maximum range is 100 meters. Given the average vehicle is between 1-3 meters tall and the height of the field-of-view at the maximum range is over 17 meters, it is unlikely that the radar field-of-view will feature more dynamic targets than static targets when it is not directly obstructed.

# C. Problem Formulation

Given a radar datagram D, estimate the radar ego-velocity along the planar ground surface,  ${}^{\mathcal{D}}\mathbf{v} = [{}^{\mathcal{D}}v_x {}^{\mathcal{D}}v_y {}^{\mathcal{D}}v_z]^\mathsf{T}$ , where  ${}^{\mathcal{D}}v_z \approx 0$  by assumption.

# IV. EGO-VELOCITY ESTIMATION ALGORITHM

# A. Modeling Doppler Velocity: Issues in Existing Methods

The Doppler velocity of a target is measured by the frequency shift of the reflected signal returned to the radar relative to the original signal. As the Doppler frequency shift is only induced by velocity in the direction of signal propagation, velocity tangent to the signal propagation has no effect, and hence the Doppler velocity of a target is the scalar projection of the target's relative velocity onto the radial vector to the target. The radial vector to a target is calculated via a coordinate transformation from the radar's observed spherical coordinates into the Cartesian coordinate frame  $\{\mathcal{D}\}$ ,  $\mathbf{r}_i = \begin{bmatrix} r_i \cos \theta_i \cos \phi_i \\ r_i \sin \theta_i \cos \phi_i \\ -r_i \sin \phi_i \end{bmatrix}$ . Note the negative in the z-axis coordinate is included in order to preserve the right-handedness of  $\{\mathcal{D}\}$ . For a static target detection, i.e. a

detection of a target with zero velocity of its own, the target's relative velocity is the negative of the radar ego-velocity,  $-^{\mathcal{D}}\mathbf{v}$ . Projecting the ego-velocity into the radial direction, a complete three dimensional model of the relative Doppler velocity of a static target detection is,

$$v_{r,i} = \frac{-^{\mathcal{D}} \mathbf{v} \cdot \mathbf{r}_i}{\|\mathbf{r}_i\|}$$
$$= -(^{\mathcal{D}} v_x \cos \theta_i + ^{\mathcal{D}} v_y \sin \theta_i) \cos \phi_i - ^{\mathcal{D}} v_z \sin \phi_i, \quad (2)$$

where  $\cdot$  denotes the standard vector dot product. This model can be seen depicted in Fig. 1.

In the existing approach of Kellner *et al.* [12], targets are either assumed to have no elevation, which may be reasonable for radars with very narrow elevation beam width, or that the elevation has no effect on the Doppler velocity of the target detection, which may be reasonable if the radar has low Doppler velocity measurement accuracy or resolution. This assumption results in a straightforward linear model for the Doppler velocity by setting  $\phi_i = 0$  in (2),

$$v_{r,i} = -^{\mathcal{D}} v_x \cos \theta_i - ^{\mathcal{D}} v_y \sin \theta_i, \tag{3}$$

and one can estimate the radar ego-velocity using this model by solving a system of linear equations using a weighted least squares approach,

$$\operatorname{argmin}_{\mathcal{D}_{\mathbf{V}}} \sum_{i=1}^{n} \frac{(v_{r,i} + \left[\cos \theta_{i} \sin \theta_{i} \ 0\right]^{\mathcal{D}} \mathbf{v})^{2}}{\sigma_{v_{r,i}}^{2}}.$$
 (4)

We improve upon the existing approach by considering the target elevation as in (2), however, under our assumptions we can say that  ${}^{\mathcal{D}}v_z \approx 0$ , resulting in a simplified model,

$$v_{r,i} = -(^{\mathcal{D}}v_x \cos \theta_i + ^{\mathcal{D}}v_y \sin \theta_i) \cos \phi_i. \tag{5}$$

The primary difference between the existing model (3) and the model presented here in (5) is that the existing model describes the Doppler velocity as a function of azimuth angle  $\theta_i$  in two dimensions, whereas our model describes the Doppler velocity as a surface which is a function of both the azimuth angle  $\theta_i$  and the elevation angle  $\phi_i$  in three dimensions. However, due to the sensor limitations, we are not able to directly observe the target elevations, and hence we can only see the projection of the model onto the target Doppler velocity-azimuth plane.

Upon further comparison of the models from (3) and (5) it becomes clear that the target's elevation causes a shrinking effect on the Doppler velocity since  $\cos(\phi_i) \leq 1$  in (5). Ultimately this produces a result from the least squares approach (4) which is biased towards smaller absolute ego-velocities. By accounting for the target elevations, we attempt to eliminate this source of bias.

It is worth noting that our improved model (5) is still an approximation of the complete Doppler velocity model (2) because we ignore the vertical velocity component,  ${}^{\mathcal{D}}v_z\sin(\phi_i)$ , by assumption. For most driving scenarios this component is insignificant relative to the component captured by (5), however, on very hilly terrain or when there are bumpy road conditions (e.g. speed bumps, construction sites), our model will still have some error relative to the ground truth. This error exists in both

our approach as well as the existing approach, so our approach should still perform no worse, and generally better, under such conditions.

# B. Modeling Target Types to Improve Ego-Velocity Estimation

In order to estimate the ego-velocity of the radar, it is first necessary to identify the static and dynamic targets. The static targets are model inliers and will be used to estimate the ego-velocity. The dynamic targets, in general, appear as outliers to the model and must be accounted for in order to minimize their effect on the solution.

We note that it is possible to recognize target types (e.g. static vs dynamic, elevated vs not elevated) by observing the values of radial velocity. Let us begin by making use of the zero-elevation model from (3) and then we will observe the discrepancy between the model and the observation to identify target types. Given the estimated radar ego-velocity  $^{\mathcal{D}}\hat{\mathbf{v}}$ , we have the estimated zero-elevation Doppler velocity function which maps to the estimated Doppler velocity of a static, non-elevated target from a target's azimuth angle  $\theta_i$ 

$$\hat{v}_r(\theta_i \mid {}^{\mathcal{D}}\hat{\mathbf{v}}) = -{}^{\mathcal{D}}\hat{v}_x \cos(\theta_i) - {}^{\mathcal{D}}\hat{v}_y \sin(\theta_i), \tag{6}$$

where  ${}^{\mathcal{D}}\hat{v}_x$  and  ${}^{\mathcal{D}}\hat{v}_y$  are the components of  ${}^{\mathcal{D}}\hat{\mathbf{v}}$  and  $(\cdot|\cdot)$  is the conditional statement of the random variable with condition on the right side of |. We note that the residual Doppler velocity of a target detection relative to this function is,

$$\epsilon_i = v_{r,i} - \hat{v}_r(\theta_i \mid {}^{\mathcal{D}}\hat{\mathbf{v}}). \tag{7}$$

In our design, we can take account for the target type and elevation by applying a nonlinear cost function to this residual which approximates the Doppler velocity residual of the target relative to the improved model in (5). Note that (5) cannot be directly used because we do not have reading  $\phi_i$  due to the fact that the radar can only perform horizontal scanning. The cost function can be adopted in an optimal parameter estimation later to recover the value of the ego-velocity.

Let us assume for now that  $\hat{v}_r(\theta_i \mid {}^{\mathcal{D}}\hat{\mathbf{v}}) \leq 0$  for a given target  $s_i$ , which is generally the case when the radar is moving in the forward direction. We model three different cases which are visualized in Fig. 2:

**Type I:** If a dynamic target is moving towards the radar in the radial direction, then it will appear to be moving towards the radar at higher (i.e. more negative) speed than a static target would. Therefore, correspondingly, if the target's Doppler velocity is less than the estimated zero-elevation Doppler velocity profile function i.e.

$$v_{r,i} < \hat{v}_r(\theta_i \mid {}^{\mathcal{D}}\hat{\mathbf{v}}), \tag{8}$$

then it is safe to assume the target to be a dynamic target moving towards the radar in the radial direction and its cost is simply the residual  $\epsilon_i$ .

**Type II:** If a target is static but elevated, then its Doppler velocity will be a product of the zero-elevation Doppler velocity profile function and the elevation effect of the target,

$$\hat{v}_r(\theta_i \mid {}^{\mathcal{D}}\hat{\mathbf{v}})\cos(\phi_i).$$
 (9)

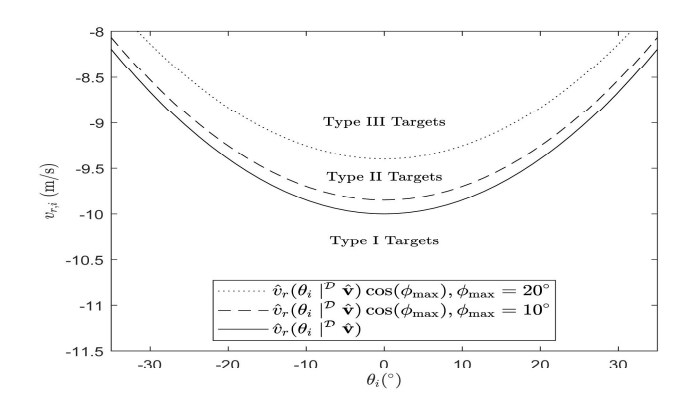


Fig. 2. Visualization of the EBAC function cases and modeling for  ${}^{\mathcal{D}}v_x=10$  m/s and  ${}^{\mathcal{D}}v_y=0$  m/s. The solid curve,  $\hat{v}_r(\theta_i\mid{}^{\mathcal{D}}\hat{\mathbf{v}})$  is the zero-elevation Doppler velocity profile function and the dashed curve  $(\phi_{\max}=10^\circ)$  and dotted curve  $(\phi_{\max}=20^\circ)$  correspond to the maximum elevation effect. A target is Type I if it is in the region below the zero-elevation Doppler velocity curve. A target is Type II if it is located in the region between the zero-elevation Doppler velocity profile function curve and the maximum elevation effect curve corresponding to  $\phi_{\max}$ . A target is Type III if it is located in the region above the maximum elevation effect curve corresponding to  $\phi_{\max}$ .

Due to the fact that we know beam width and radar resolution, we know the maximum vertical spanning angle  $\phi_{\max}$  of the radar. Further, we know that  $0 \le \cos(\phi_i) \le 1$  for  $\phi_i \in [-\phi_{\max}, \phi_{\max}]$ , therefore, we can say that if the Doppler velocity of a target is between the zero-elevation Doppler velocity profile function and its product with maximum elevation effect defined in (9) i.e.

$$\hat{v}_r(\theta_i \mid {}^{\mathcal{D}}\hat{\mathbf{v}})\cos(\phi_{\max}) \ge v_{r,i} \ge \hat{v}_r(\theta_i \mid {}^{\mathcal{D}}\hat{\mathbf{v}}), \tag{10}$$

then it is likely to be a static target (i.e. background object). For such targets, we set their cost to be 0 since these target's are within the tolerable range of our improved model (5).

**Type III:** For the rest, the target is assumed to be a dynamic target moving away from the radar in the radial direction and the cost is the residual plus a correction factor which maintains the continuity of the cost function across all three target detection types by accounting for the elevation effect tolerance for the Type II target detections, i.e.

$$\epsilon_i + (1 - \cos(\phi_{\text{max}}))\hat{v}_r(\theta_i \mid {}^{\mathcal{D}}\hat{\mathbf{v}}).$$
 (11)

Bringing this all together, we have a piecewise cost function which we will refer to as the Elevation and Background Aware Doppler Cost (EBAC) function,

$$f(\epsilon_{i}, v_{r,i}, \theta_{i} \mid {}^{\mathcal{D}}\hat{\mathbf{v}})$$

$$= \begin{cases} \epsilon_{i}, & \text{if } v_{r,i} < \hat{v}_{r}(\theta_{i}) \\ 0, & \text{if } \hat{v}_{r}(\theta_{i}) \cos(\phi_{\max}) \ge v_{r,i} \ge \hat{v}_{r}(\theta_{i}) \\ \epsilon_{i} + (1 - \cos(\phi_{\max}))\hat{v}_{r}(\theta_{i}), & \text{otherwise,} \end{cases}$$
(12)

where  $\hat{v}_r(\theta_i)$  is used in place of  $\hat{v}_r(\theta_i \mid {}^{\mathcal{D}}\hat{\mathbf{v}})$  in order to conserve space. It is worth noting that EBAC function in (12) only depends on a known prior  $\phi_{\max}$  instead of the unknown target elevation reading.

The EBAC function can be easily extended to the case where  $\hat{v}_r(\theta_i \mid {}^{\mathcal{D}}\hat{\mathbf{v}}) > 0$  by mirroring the direction of the described inequalities in (12), however, we omit the full derivation in favor of deriving the most common case for brevity. While

the three described cases are generally sufficient for the most common situation of the radar moving in the forward direction, ultimately, the full EBAC function should have six cases, the three described here for  $\hat{v}_r(\theta_i \mid {}^{\mathcal{D}}\hat{\mathbf{v}}) \leq 0$  and three more with mirrored inequalities for  $\hat{v}_r(\theta_i \mid {}^{\mathcal{D}}\hat{\mathbf{v}}) > 0$ .

As the first step in our algorithm, we employ the RANSAC algorithm to find the largest inlier set to our improved model (5), where the absolute value of the EBAC function serves as the error metric indicating the distance of a given target detection from this model. In each RANSAC iteration we select two random targets from D and find an exact solution to (4). We use this solution as the estimated ego-velocity  ${}^{\mathcal{D}}\hat{\mathbf{v}}$  to construct the zero-elevation Doppler velocity function (6) and thereby instantiate our model. For each target in D, we consider it an inlier if the absolute value of the EBAC function is less than some threshold which we empirically choose to be  $2.5\sigma_{v_{r,i}}$ . This serves as a probability threshold for admitting target detections which are on the borderline between static and dynamic target detections as inliers. After some number of iterations, we take the solution with the largest number of inliers and consider it to be the RANSAC solution.

Following the completion of the RANSAC algorithm iterations, we construct a set of radar detections  $D_B$  which is a subset of the original radar datagram D consisting of the static inlier target detections to the RANSAC solution. We will use  $D_B$  in the subsequent optimal parameter estimation to determine the radar ego-velocity. One may also construct a set consisting of the dynamic outlier targets,  $D_F = D \backslash D_B$ , which is not utilized in this work but may be useful for other radar works related to dynamic target identification and tracking.

# C. Estimating the Radar Ego-Velocity

Given the set of static, background target detections  $D_B$  we can finally estimate the radar ego-velocity by performing an optimal parameter estimation for our improved model (5).

In order to account for the noise which is present in both the independent variable  $\theta_i$  as well as the dependent variable  $v_{r,i}$  we make use of Orthogonal Distance Regression (ODR) [15],

$$\begin{aligned} \operatorname{argmin}_{\mathcal{D}_{\mathbf{V},\boldsymbol{\delta},\boldsymbol{\phi}}} \sum_{i=1}^{n} & \frac{(v_{r,i} - \hat{v}_{r}(\theta_{i} + \delta_{i} \mid {}^{\mathcal{D}}\mathbf{v})\cos\phi_{i})^{2}}{\sigma_{v_{r,i}}^{2}} + \frac{\delta_{i}^{2}}{\sigma_{\theta,i}^{2}} \\ & + \lambda \frac{(\hat{v}_{r}(\theta_{i} + \delta_{i} \mid {}^{\mathcal{D}}\mathbf{v})(1 - \cos\phi_{i}))^{2}}{\sigma_{v_{r,i}}^{2}}, \\ \operatorname{subject to} & 0 \leq \phi_{i} \leq \phi_{\max}, \ i = 1, \ldots, n, \end{aligned}$$

where  $\delta_i$  is the estimated error of the target azimuth observation. We additionally add  $\lambda$  and its associated component as a regularization upon  $\phi_i$  which controls for the amount of variance in  $v_{r,i}$  explained by the elevation. As  $\lambda \to \infty$ ,  $\phi_i$  will be forced to zero and the model will not make account for elevation. As  $\lambda \to 0^+$ , the model will increasingly explain the variance in  $v_{r,i}$  by the elevation effects. This orthogonal distance regression also provides a potentially useful side-product, resulting from the use of the target elevation in the optimization, in the form the estimated absolute values of the target elevations.

# V. EXPERIMENTS

The presented algorithms have been tested and validated using simulated data as well as real-world data collected from our Continental ARS430 Doppler radar which is mounted to front of a 2017 Chevy Bolt EV designed for autonomous driving. All of the algorithms have been developed as a set of Robotic Operating System (ROS) [20] modules in C++ using Ceres Solver [21] for solving the regressions and Eigen [22] for matrix computations. We compare the results of our algorithm to that of Kellner *et al.* [12].

### A. Simulation

Due to the wide array of parameters affecting the algorithm, we make use of simulation in order to provide as much coverage of these parameters as possible. We create a simulated radar module in ROS which emulates the performance and characteristics of a real world Doppler radar by generating simulated radar datagrams. For each simulation, we generate 10000 simulated radar datagrams with 150 targets. We send the simulated radar datagrams as input into each algorithm identically, and compute the mean and standard deviation of the magnitude of the ego-velocity estimation error

$$e_v = \|^{\mathcal{D}} \hat{\mathbf{v}} - {}^{\mathcal{D}} \mathbf{v} \|. \tag{14}$$

For the mean errors smaller values are preferred as they indicate a lower bias of the algorithm's estimations and smaller standard deviations are preferred as they indicate superior stability of the algorithm's estimations.

To generate a static target  $s_i$ , we generate the target range, azimuth, and elevation as random variables such that  $r_i \sim U(5 \text{ m}, 100 \text{ m}), \ \theta_i \sim U(-60^\circ, 60^\circ), \ \text{and} \ \phi_i \sim U(-10^\circ, 10^\circ), \ \text{where} \ U(\cdot, \cdot)$  is the continuous uniform distribution. We compute  $v_{r,i}$  for each target as in (2).

To generate a dynamic target  $s_i$ , recall that the fixed global coordinate system  $\{\mathcal{W}\}$  is aligned with the radar coordinate system  $\{\mathcal{D}\}$  at its initial position. The distribution of dynamic target positions and velocities will be defined in the global coordinate system  $\{W\}$  on a case-by-case basis for a given simulation scenario. The dynamic target positions and velocities are transformed from  $\{\mathcal{W}\}$  into  $\{\mathcal{D}\}$  in order to populate the simulated radar datagram. The target range and azimuth are computed by converting the target positions in  $\{\mathcal{D}\}$  into the polar coordinate representation. We set the target elevation  $\phi_i = 0$ since we assume that dynamic targets will be moving along the same planar surface as the vehicle and their height will generally be insignificant compared to their range. As previously discussed, the Doppler velocity of a target is the scalar projection of the target's relative velocity onto the radial vector to the target. Let  ${}^{\mathcal{D}}\mathbf{v}_i = [{}^{\mathcal{D}}v_{x,i} {}^{\mathcal{D}}v_{y,i} \ 0]^\mathsf{T}$  be the velocity of the target  $s_i$  from the radar perspective, then the relative velocity of the target is  ${}^{\mathcal{D}}\mathbf{v}_i - {}^{\mathcal{D}}\mathbf{v}$ . Therefore the Doppler velocity of the dynamic target is computed to be

$$v_{r,i} = \frac{({}^{\mathcal{D}}\mathbf{v}_i - {}^{\mathcal{D}}\mathbf{v}) \cdot \mathbf{r}_i}{\|\mathbf{r}_i\|}$$
$$= (({}^{\mathcal{D}}v_{x,i} - {}^{\mathcal{D}}v_x)\cos\theta_i + ({}^{\mathcal{D}}v_{y,i} - {}^{\mathcal{D}}v_y)\sin\theta_i)\cos\phi_i,$$
(15)

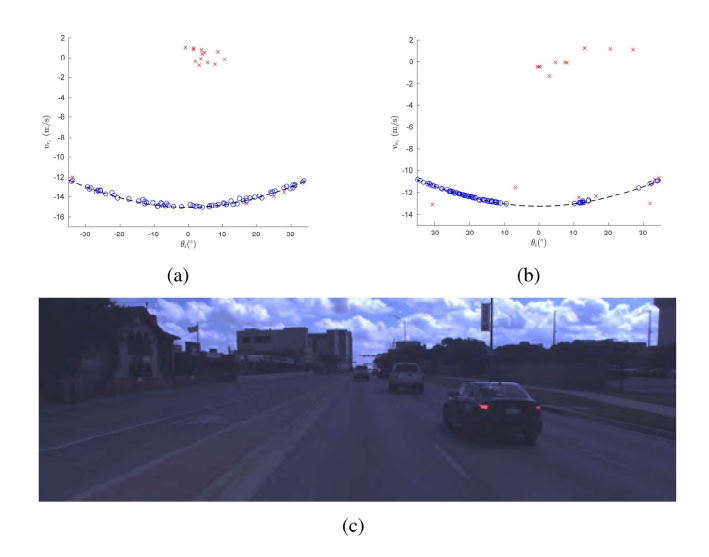


Fig. 3. A comparison between simulated radar datagram and real radar datagram featuring both static and dynamic targets. (a) Simulated datagram: target Doppler velocity vs. azimuth plot. (b) Real datagram: target Doppler velocity vs. azimuth plot. Both static and dynamic targets are collected from the physical experiments. (c) The camera image corresponding to the real radar datagram. (a) and (b) are cropped to align with the image bounds, blue os indicate the static inlier detections, red ×s indicate dynamic or outlier detections, and the dashed black line is the zero-elevation Doppler function.

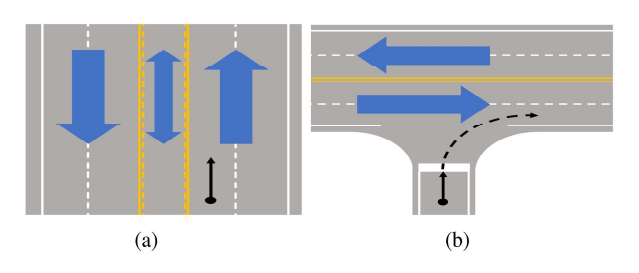


Fig. 4. Diagrams of simulated scenarios where the blue arrows represent the flow of traffic in a given group of lanes. (a) The solid black line represents the radar trajectory for Scenario 1. (b) The solid black line represents the radar trajectory for Scenario 2, and the dashed black line represents the radar trajectory for Scenario 3. Note that the figures are for visual reference and are not necessarily drawn to scale.

For all the targets in our simulated radar datagram, we simulate the observation noise of the measurements. For a given target  $s_i$  in the radar datagram we let the azimuth observation noise be a random variable  $\delta_i \sim N(0,\sigma_{\theta,i})$  where  $\sigma_{\theta,i}=1^\circ$  and the Doppler velocity observation noise be a random variable  $\epsilon_i \sim N(0,\sigma_{v_{r,i}})$  where  $\sigma_{v_{r,i}}=0.1\text{m/s}.$   $N(\mu,\sigma)$  is the normal distribution with mean  $\mu$  and standard deviation  $\sigma.$   $\delta_i$  and  $\epsilon_i$  are added to  $\theta_i$  and  $v_{r,i}$  respectively. Note that we do not define the noise in  $r_i$  as it is not used in our estimation process nor do we define the elevation noise as it is not considered to be an observation and is used only exactly to compute the ground truth target Doppler velocity.

Fig. 3 demonstrates a sample comparison of our real world data versus our simulated data in the target azimuth vs target Doppler velocity space. It is clear that our simulation is very faithful and covers the key characteristics of the radar datagram. In order to validate the robustness of our algorithm to dynamic target detections we construct three representative scenarios (see Fig. 4) to emulate real world driving situations.

**Scenario 1**: we simulate the case of driving straight along a bidirectional five-lane roadway with two lanes in each direction and a bidirectional center turning lane. We set the radar ego-velocity to be such that  ${}^{\mathcal{D}}v_x=15$  m/s and  ${}^{\mathcal{D}}v_y=0$  m/s and we vary the ratio of dynamic to static targets. We generate a given dynamic target  $s_i$  to be positioned in the two right-most lanes (the radar's lane and the lane to the right) with probability 47.5%, the two left-lanes with probability 47.5%, or the center turning lane with probability 5%. Given a dynamic target  $s_i$ , we set its velocity from the global coordinate perspective to be such that  ${}^{\mathcal{W}}v_{y,i}=0$  m/s and  ${}^{\mathcal{W}}v_{x,i}\sim U(14$  m/s, 16 m/s) for a dynamic target in the two right-most lanes,  ${}^{\mathcal{W}}v_{x,i}\sim$ U(-16 m/s, -14 m/s) for a dynamic target in the two left-most lanes, and  ${}^{\mathcal{W}}v_{x,i} \sim U(-16 \text{ m/s}, 16 \text{ m/s})$  for a dynamic target in the center turning lane. In fact, the example in Fig. 3(c) is similar to Scenario 1 without opposite traffic.

Scenario 2: we simulate the case of approaching a stop at a four lane intersection with cross traffic. We set the radar ego-velocity to be such that  ${}^{\mathcal{D}}v_x=5$  m/s and  ${}^{\mathcal{D}}v_y=0$  m/s and we vary the ratio of dynamic to static targets. We generate a given dynamic target  $s_i$  to be positioned in either the two nearest crossing lanes or the two furthest crossing lanes with equal probability of 50%. Given a dynamic target  $s_i$ , we set its velocity from the fixed global coordinate perspective such that  ${}^{\mathcal{W}}v_{x,i}=0$  m/s and  ${}^{\mathcal{W}}v_{y,i}\sim U(14$  m/s, 16 m/s) for a dynamic target in the two nearest crossing lanes and  ${}^{\mathcal{W}}v_{y,i}\sim U(-14$  m/s, -16 m/s) for a dynamic target in the two furthest crossing lanes.

Scenario 3: we simulate the case making a right turn at a four lane intersection with cross traffic. We set the radar egovelocity to be such that  $\|^{\mathcal{D}}\mathbf{v}\| = 5$  m/s and we vary the ratio of dynamic to static targets. The radar begins facing the cross traffic and makes a right turn with a radius 10 meters and ends parallel with the cross traffic in the rightmost lane. To execute the turn we provide a steering angle of  $20^{\circ}$  which corresponds to a longitudinal velocity of  $^{\mathcal{D}}v_x \approx 4.7$  m/s and a lateral velocity of  $^{\mathcal{D}}v_y \approx 1.7$  m/s. The dynamic targets are generated as previously described in Scenario 2.

The results of the simulations of Scenarios 1, 2, and 3 are detailed in Fig. 5. The results show that our algorithm offers an improvement to the existing approach for situations where there are elevated target detections. Our algorithm reduces the magnitude of the velocity estimation error by an average of 49%, 34%, and 33% on average for radar datagrams containing up to 50% dynamic targets for Scenario 1, Scenario 2, and Scenario 3 respectively. Further, our algorithm reduces the standard deviation of the magnitude of the velocity estimation errors by approximately 12%, 12%, and 11% for up to 50% outliers in Scenario 1, Scenario 2, and Scenario 3 respectively. Our algorithm offers similar robustness to the existing approach, working reliably for up to 50% dynamic targets. Beyond 50% dynamic targets, both the existing approach and our approach begin to breakdown and select incorrect static inlier sets in the RANSAC segmentation step.

The three scenarios represent three extreme cases in radar applications. Due to the fact that the ego-vehicle and other vehicles are either co-directional or in the opposite direction, Scenario 1's relative velocity to other vehicles is very close

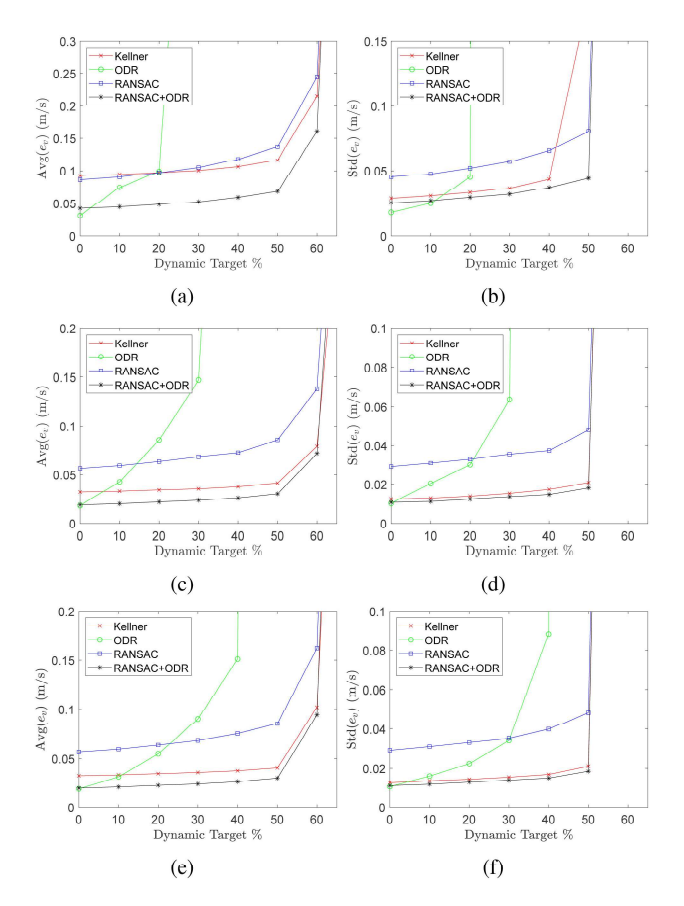


Fig. 5. Ratio of dynamic targets versus (a) the mean and (b) the standard deviation of the velocity error magnitude  $e_v$  for simulation Scenario 1, (c) the mean and (d) the standard deviation of the velocity error magnitude  $e_v$  for simulation Scenario 2, (e) the mean and (f) standard deviation of the velocity error magnitude  $e_v$  for simulation Scenario 3.

to Doppler velocity. In fact, Scenario 1 is arguably the most common driving scenario. The fact that our estimation method reduces the magnitude of the velocity estimation error by an average of 49% is very encouraging. In Scenario 2, the egovehicle is perpendicular to other vehicles when the Doppler velocity is much less affected by the relative velocity to other vehicles. All other driving scenarios can be considered as the intermediate scenarios between the two representative extreme scenarios here. Scenario 3 demonstrates that the performance is not degraded by lateral motions of the radar. The right turn into cross traffic generally requires the largest steering angle under normal driving conditions, therefore all other turning scenarios fall between the linear trajectory in Scenario 2 and the sharp turning trajectory in Scenario 3.

# B. Physical Experiments With an Autonomous Vehicle

In order to verify the algorithm performance beyond the idealized simulation environment and under real-world conditions, we mount Continental ARS430 radar to the front bumper of a 2017 Chevrolet Bolt EV (see Fig. 1) and perform physical experiments. We drive our vehicle in a typical urban scene featuring elevated natural targets such as tall trees and elevated infrastructure such as multi-story buildings and street lights which is depicted in Fig. 6. We first record a one minute dataset with the vehicle parked and thus the radar stationary. For subsequent





Fig. 6. A sample of camera image data captured simultaneously with the radar data by our autonomous vehicle platform during the physical experiments. The colored points are the radar target detections projected into the image coordinates. Note that the target elevations are the absolute elevations as estimated by (13). The point color coding indicates the target's height in meters relative to the horizontal plane. Projected images are generated by RViz.

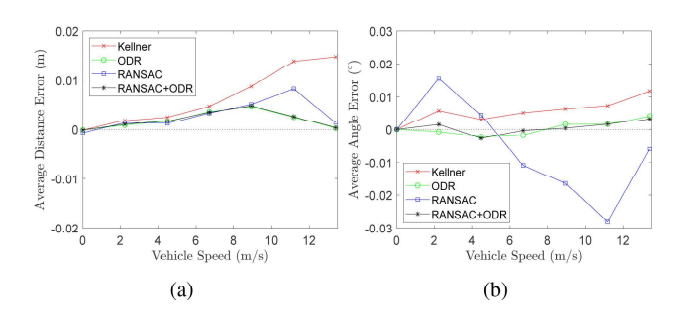


Fig. 7. The vehicle speed in meters per second versus (a) the mean distance integration error per radar datagram and (b) the mean angular integration error per radar datagram.

trials we repeat a linear trajectory approximately 150 meters long through the scene varying the vehicle speed using the vehicle cruise control, and therefore the radar's longitudinal velocity, for each trial. We apply the radar ego-velocity estimations to the same single-track kinematic vehicle model with the Ackermann steering condition as Kellner et al. [12] and integrate over the trajectory. Due to the compounding effects of integration of even slight errors in the lateral velocity to the overall displacement of the estimated trajectory, we separately estimate the integrated trajectory distance and the integrated trajectory rotation. We compute the error of the estimated trajectory distance and rotation by comparison to GPS/INS data collected simultaneously from our Novatel PwrPak7 GNSS/INS. In order to normalize the errors we divide the errors by the total number of radar datagrams processed for the trajectory. Results for these physical experiments are presented in Fig. 7. Again, our RANSAC+ODR method has significantly outperformed its counterparts. It consistently has the smallest distance error and angular error across a variety of vehicle speeds. Whereas the existing approach will accumulate distance error proportional with the vehicle speed due to its inherent bias, our approach is not significantly affected as the vehicle speed increases.

We additionally present a sample output of our algorithm's elevation estimation and target type separation for real-world data collected on our autonomous vehicle platform. In Figs. 6 and 8 we show the projected radar target detections into the camera image coordinates and validate that the target elevation estimations as determined by (13) appear visually reasonable. As shown in Fig. 8, our algorithm has successfully identified the three types of targets described in Section IV-B.

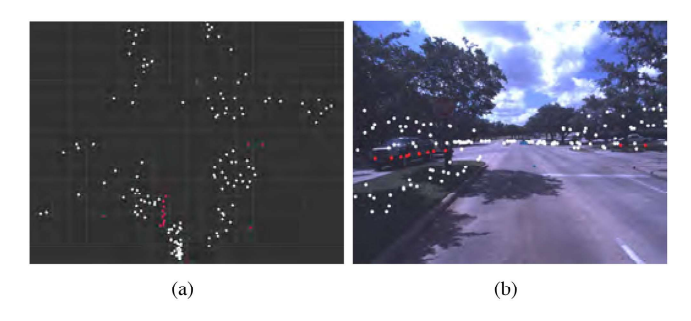


Fig. 8. An example of our target type identification on real data collected at a four-way intersection. White points are static, Type II target detections. Red points are dynamic, Type I (moving towards the radar) detections. Blue points are dynamic, Type III (moving away from the radar) detections. Target coordinates are rendered in  $\{\mathcal{D}\}$  with the underlying grid-squares having 5 m spacing. (a) Birds-eye view of the radar coordinate system. (b) A sample of camera image data captured simultaneously with the radar data by our autonomous vehicle platform. The colored points are the radar target detections projected into the image coordinates. Note that the target elevations are the absolute elevations as estimated by (13). Images are generated by RViz.

### VI. CONCLUSION AND FUTURE WORKS

We reported our algorithm design to improve ego-velocity estimation for a low-cost Doppler automotive radar which is widely used in autonomous driving and ADAS. The existing state-of-the-art assumed that all objects are located close to the ground and hence treat them as co-planar objects. However, elevated objects such as buildings and tall trees commonly exist along the roadside which inevitably cause radar ego-velocity estimation to be deviated from its true value. We modeled and analyzed the issue and proposed a cost function to capture the discrepancy which results in an optimization framework that can recognize object types and allow us to obtain accurate ego-vehicle estimation. Combining the new framework with RANSAC, our method reduced ego-velocity estimation error while improving in robustness and reducing error variance. Our simulation and physical experiment on our autonomous vehicle validated our analysis and design.

In the future, we will further develop feature recognition algorithms to recognize other ground features such as vertical building facades or curb corners based on raw radar datagrams. This will allow us to build high-level landmarks in radar-based SLAM approaches. In addition, we will design cross-modality sensor fusion with LIDAR and other sensors.

### ACKNOWLEDGMENT

We thank M. Boyle for his advisory inputs for building autonomous vehicles. We are also grateful to S. Yeh, D. Wang, A. Angert, S. Xie, F. Guo, Y. Jiang, and C. Qian for their inputs and feedback.

### REFERENCES

- [1] D. Langer, "An integrated MMW radar system for outdoor navigation," in *Proc. IEEE Int. Conf. Robot. Automat.*, 1996, pp. 417–422.
- [2] S. Clark and H. Durrant-Whyte, "Autonomous land vehicle navigation using millimeter wave radar," in *Proc. IEEE Int. Conf. Robot. Automat.*, 1998, pp. 3697–3702.
- [3] S. Clark and G. Dissanayake, "Simultaneous localisation and map building using millimetre wave radar to extract natural features," in *Proc. IEEE Int. Conf. Robot. Automat.*, 1999, pp. 1316–1321.
- [4] M. W. M. G. Dissanayake, P. Newman, S. Clark, H. F. Durrant-Whyte, and M. Csorba, "A solution to the simultaneous localization and map building (SLAM) problem," *IEEE Trans. Robot. Automat.*, vol. 17, no. 3, pp. 229–241, Jun. 2001.
- [5] F. Schuster, C. G. Keller, M. Rapp, M. Haueis, and C. Curio, "Landmark based radar SLAM using graph optimization," in *Proc. IEEE 19th Int. Conf. Intell. Transp. Syst.*, 2016, pp. 2559–2564.
- [6] S. Thrun and M. Montemerlo, "The graph SLAM algorithm with applications to large-scale mapping of urban structures," *Int. J. Robot. Res.*, vol. 25, no. 5/6, pp. 403–429, 2006.
- [7] P. Checchin, F. Gérossier, C. Blanc, R. Chapuis, and L. Trassoudaine, "Radar scan matching SLAM using the Fourier-Mellin transform," in *Proc. Field Service Robot.*, 2010, pp. 151–161.
- [8] D. Vivet, P. Checchin, and R. Chapuis, "Radar-only localization and mapping for ground vehicle at high speed and for riverside boat," in *Proc. IEEE Int. Conf. Robot. Automat.*, 2012, pp. 2618–2624.
- [9] S. H. Cen and P. Newman, "Precise ego-motion estimation with millimeter-wave radar under diverse and challenging conditions," in *Proc. IEEE Int. Conf. Robot. Automat.*, 2018, pp. 6045–6052.
- [10] S. H. Cen and P. Newman, "Radar-only ego-motion estimation in difficult settings via graph matching," in *Proc. IEEE Int. Conf. Robot. Automat.*, 2019, pp. 298–304.
- [11] K. Werber, J. Klappstein, J. Dickmann, and C. Waldschmidt, "Association of straight radar landmarks for vehicle self-localization," in *Proc. IEEE Intell. Veh. Symp.*, 2019, pp. 736–743.
- [12] D. Kellner, M. Barjenbruch, J. Klappstein, J. Dickmann, and K. Dietmayer, "Instantaneous ego-motion estimation using doppler radar," in *Proc. IEEE* 16th Int. Conf. Intell. Transp. Syst., 2013, pp. 869–874.
- [13] M. A. Fischler and R. C. Bolles, "Random sample consensus: A paradigm for model fitting with applications to image analysis and automated cartography," *Commun. ACM*, vol. 24, no. 6, pp. 381–395, 1981.
- [14] D. Kellner, M. Barjenbruch, J. Klappstein, J. Dickmann, and K. Dietmayer, "Instantaneous ego-motion estimation using multiple Doppler radars," in *Proc. IEEE Int. Conf. Robot. Automat.*, 2014, pp. 1592–1597.
- [15] P. T. Boggs and J. E. Rogers, "Orthogonal distance regression," Contemporary Math., vol. 112, pp. 183–194, 1990.
- [16] M. Steiner, O. Hammouda, and C. Waldschmidt, "Ego-motion estimation using distributed single-channel radar sensors," in *Proc. IEEE MTT-S Int. Conf. Microw. Intell. Mobility*, 2018, pp. 1–4.
- [17] H.-W. Cho, S. Choi, Y.-R. Cho, and J. Kim, "Deep complex-valued network for ego-velocity estimation with millimeter-wave radar," in *Proc. IEEE SENSORS*, 2020, pp. 1–4.
- [18] H.-W. Cho, S. Choi, Y.-R. Cho, and J. Kim, "Complex-valued channel attention and application in ego-velocity estimation with automotive radar," *IEEE Access*, vol. 9, pp. 17717–17727, 2021.
- [19] C. D. Monaco and S. N. Brennan, "RADARODO: Ego-motion estimation from Doppler and spatial data in radar images," *IEEE Trans. Intell. Veh.*, vol. 5, no. 3, pp. 475–484, Sep. 2020.
- [20] M. Quigley et al., "ROS: An open-source robot operating system," in Proc. ICRA Workshop Open Source Softw., Kobe, Japan, 2009, Art. no. 5.
- [21] S. Agarwal and K. Mierle, and Others, "Ceres solver," Mar. 2022. [Online]. Available: https://github.com/ceres-solver/ceres-solver
- [22] G. Guennebaud *et al.*, "Eigen v3," 2010. [Online]. Available: http://eigen. tuxfamily.org